3D-Printed Carbons with Improved Properties and Oxidation Resistance

Pauline Blyweert, Nicolas Vincent, Vanessa Fierro, Alain Celzard

3D-printed carbons with improved properties and oxidation resistance

*Pauline Blyweert †, Vincent Nicolas †, Vanessa Fierro †, Alain Celzard †,‡,**

† Université de Lorraine, CNRS, IJL, F-88000 Epinal, France

‡ Institut Universitaire de France (IUF)

KEYWORDS

*Corresponding author: Pr. Alain Celzard (alain.celzard@univ-lorraine.fr), Université de Lorraine

Stereolithography, Porous carbon, Bio-based monomers, Tannin, Vanillin

ABSTRACT

In this paper, we show preparation and characteristics of new 3D-printed porous carbons obtained by stereolithography (SLA) of a precursor resin followed by heat treatment. Their physical and textural properties can be tuned by using chemically modified bio-based aromatic precursors as monomers. Thus, vanillin and polyflavonoids such as mimosa tannin can be used together as building blocks for SLA materials when functionalized with methacrylate groups by a solvent-free technique and mixed with a photosensitive resin. Adjusting the photosensitive formulations led to a high thermal stability and an increase in carbon yield up to 27%. The corresponding dense porous carbon materials showed outstanding mechanical properties, far exceeding those of other SLA-printed carbons and carbon foams, and a very low surface area, which improves their oxidation resistance compared to acrylate-tannin-derived carbon or activated carbons. This new approach to architecturally engineered carbons with tailored properties can therefore be used for the promising design of catalyst supports or sodium-ion batteries.

INTRODUCTION

On-demand manufacturing of porous carbon materials with complex architectures, accurate dimensions, and given performances in specific environments is an emerging challenge [1,2]. This is especially true when using a precise and energy-efficient additive manufacturing technology such as laser stereolithography (SLA), which relies on the photoreactivity of a liquid resin [3,4].

Since pure carbon is not photopolymerizable, most SLA-printed carbon materials are obtained by printing a photocurable carbon precursor, followed by heat treatment. Previous studies have reported the use of commercially available photocurable resins based on (meth)acrylates followed by a pyrolysis step to obtain highly porous carbon materials with various pores sizes [5–10]. In general, these resins are derived from fossil resources and, in most cases, the carbon yield remains particularly low and the architectures undergo significant volume shrinkage during the thermal treatment [11,12]. Therefore, many efforts have been made to develop bio-based alternatives to produce 3D-printed porous carbon with attractive yield, reduced shrinkage, and good mechanical properties [13,14]. In this context, mimosa tannin has been identified as a suitable bio-based precursor to achieve such a specification, in particular with properties that can be adapted to energy and environmental applications such as electromagnetic absorption or catalysis, among others.

However, as tannin is not soluble in acrylate resins, the viscosity of the obtained dispersion limits its incorporation into the photoreactive resin to less than 30 wt.%. Consequently, this limits the final carbon yield too [15]. It is thus of interest to design a bio-based aromatic monomer with high solubility in - or compatibility with - acrylate to improve the carbon yield and the mechanical properties of the resulting 3D-printed carbon compared to 3D carbon derived from acrylate-tannin photosensitive resins.[13,14]

In recent years, significant work has been done to develop bio-based vinyl ester resins (VERs) from natural phenolic compounds such as vanillin [16–19]. Vanillin, as a natural biomass-derived molecule, has proven to be a perfect candidate for use in VERs and stereolithographic printing [20]. Indeed, when chemically modified with acrylate moieties using a sustainable approach (no solvent, reactive byproducts, use of small amounts of catalyst, and moderate temperatures) [21], the monomer (vanillin methacrylate) becomes soluble in acrylate media. The aromatic character of vanillin provides structural rigidity and thermal stability to the polymer network, leading to a mechanical improvement of the 3D-printed structure [20,22].

Similar to vanillin, the rich and complex structure of polyflavonoids allows for chemical modifications that can tune their properties [23]. The hydrophilic nature of polyflavonoids makes them incompatible with hydrophobic polymers. Adding acrylate moieties to polyflavonoids such as tannin or lignin improved the compatibility of such bio-based molecules with PLA [24] and acrylate resin for stereolithographic 3D printing, respectively. Thus, due to the reactivity of flavonoids, the mechanical properties of the printed specimens could be improved [25–28].

To the best of our knowledge, the use and combination of vanillin, tannin, or acylated tannins, and their investigation as photocurable components to produce porous carbon materials has never been studied so far. In this paper, we describe a new route to use vanillin and mimosa tannin as raw materials for the design of stereolithographically 3D-printed porous carbons that have higher carbon yield after pyrolysis and superior mechanical characteristics. The present results are discussed on the basis of structural, textural, and physical characterization of the investigated materials.

EXPERIMENTAL SECTION

Materials

Mimosa tannin extract (Fintan OP) was kindly provided by SilvaChimica (St Michele Mondovi, Italy), and vanillin (4-hydroxy-3-methoxybenzyl alcohol) was courtesy of Solvay (Solvay Group, France). Methacrylic anhydride (94%) used to acetylate vanillin and tannin, as well as 4-dimethylaminopyridine (DMAP, 99%), a catalyst for acylation, were purchased from Sigma Aldrich.

Hexanediol diacrylate (HDDA, SR238), pentaerythritol tetraacrylate (SR295) and acrylate oligomer (CN154 CG) were kindly provided by Sartomer (Arkema Group, France). Bis(2,4,6-trimethylbenzoyl)phenylphosphine oxide (BAPO) was supplied by Lambson (Arkema Group, England).

All products were used as received, without further purification. It may be useful to point out here that tannin and vanillin are industrial materials, whose production is perfectly controlled and reproducible. These materials, despite their biological origin, do not suffer from the problems of heterogeneity and quality variations usually encountered with natural substances. Added in contents higher than 30% in mixture in resins allows to qualify the latter as bio-resins,[29,30] as it will be mentioned in the rest of the manuscript.

Acylation of vanillin and tannin

Vanillin methacrylate (here referred to as Vm) was synthesized according to the reaction methodology described by Basset et al. [20] and derived from Stanzione et al. [17]. Briefly, in a 3-necked round-bottom flask equipped with a magnetic stirring bar, vanillin (7.5 g) and DMAP

(0.12 g, 0.04 eq/OH) were added. The mixture was purged with nitrogen for 10 min, and then methacrylic anhydride (4.3 g, 1.2 eq/OH) was added. The reaction medium was heated to 50 °C under continuous stirring. After 24h, the system was cooled with an ice bath and the acylated vanillin was recovered from the solution by quenching with a saturated sodium carbonate solution. The precipitate was washed with water until it reached neutrality and was dried at 70 °C overnight.

Tannin methacrylate (here called Tm) was synthesized following the same protocol by introducing 5 g of tannin (0.008 mol OH /g), 0.2 g of DMAP (0.04 eq/OH) and 6 g (*i.e.*, a large excess) of methacrylic anhydride. The reaction scheme is shown in Figure 1. The acylation reaction products were characterized by FT-IR using a Frontier Spotlight 400 spectrometer (Perkin Elmer, UK) in ATR mode (4 scans at room temperature, 1 cm^{-1} resolution in the mid- IR range).

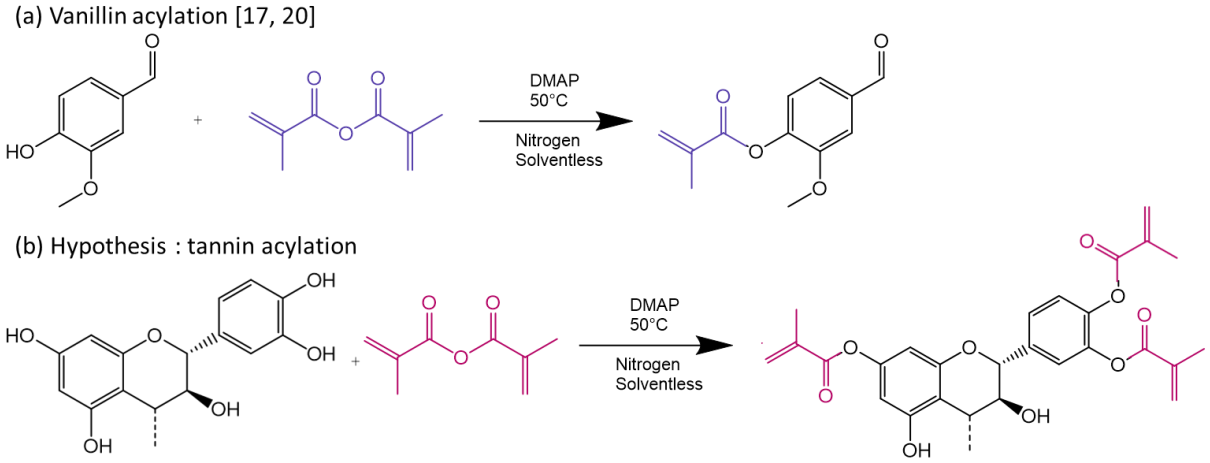

Figure 1. Reaction scheme for the preparation of: (a) vanillin methacrylate; and (b) tannin methacrylate.

Preparation of 3D-printed porous carbon architectures

A mixture of vanillin methacrylate (Vm, 45 wt.%) and either tannin (T) or tannin methacrylate (Tm) was made in a photocurable acrylate resin (A) to obtanin vanillin-tannin-acrylate resins with a fixed polyflavonoid precursor (tannin or tannin methacrylate) content of 25 wt.%.

The photocurable acrylate resin was formulated so that its viscosity matches that of commercial resins used in the DWS SLA printer (see below). This base resin is composed of acrylate monomers (SR238, SR295 and CN154 CG) and BAPO photoinitiator, added in the proportions shown in Table 1, which were homogenized with a sonotrode for 20 minutes. The resins were named after the combination of the acrylate resin and the bio-based carbon precursors.

Table 1. Formulation of the different acrylate-vanillin-tannin resins.

Ingredient (wt.%)	A-T	A-Vm-T	A-Tm	A-Vm-Tm
CN154 [a] (wt.%)	29.9	16.6	29.9	16.6
PETA [b] (wt.%)	29.9	16.6	29.9	16.6
HDDA [c] (wt.%)	14.9	8.3	14.9	8.3
BAPO [d] (wt.%)	0.3	0.3	0.3	0.3
Vanillin-methacrylate (wt.%)	-	33.1	-	33.1
Tannin (wt.%)	25	25	-	-
Tannin-methacrylate (wt.%)	-	-	25	25

[a] acrylate oligomer; [b] pentaerythritol tetraacrylate; [c] hexanediol diacrylate; [d] bis(2,4,6-trimethylbenzoyl)phenylphosphine oxide

The resultant bio-based resins were then processed with a DWS J28 (desktop SLA printer, 405 nm, DWS, Italy) to print solid cubes of side 7 mm with layers of thickness 30 µm. After printing, the architectures were washed with two isopropyl alcohol baths to remove any unreacted resin and were then post-treated in a UV oven (405 nm) for 20 minutes at room temperature.

Finally, the architectures were converted into porous carbon materials under an inert atmosphere (nitrogen at a flow rate of 75 $mL \cdot min^{-1}$) in a tubular furnace with the following thermal program: heating ramp at 1.5 $°C \cdot min^{-1}$ to 300 °C, 60 min step at 300 °C, heating at 1 $°C \cdot min^{-1}$ to 400 °C, 60 min step at 400 °C, and finally heating at 2 $°C \cdot min^{-1}$ to a final temperature of 900 °C, which was maintained for 1 h, as described elsewhere [14]. The resulting carbons were named: cA-T, cA-Vm-T, cA-Tm and cA-Vm-Tm, respectively.

Characterisation

Materials composition and reactivity

Elemental analysis (EA) of the carbon materials, *i.e.*, after 3D printing, UV curing, and pyrolysis, was performed in an Elementar Vario EL Cube analyzer, where the bulk contents of sulfur, nitrogen, hydrogen, and carbon were measured. The oxygen content was calculated by difference.

X-ray photoelectron spectroscopy (XPS) was performed using an ESCAPlus OMICRON spectrometer equipped with a non-monochromatized Mg·Kα X-ray source. Shirley-type background and quantification were processed with CASA software. Peak fitting and deconvolution of C1s and O1s signals were performed by least-square fitting using Gaussian-Lorentzian curves.

The glass transition temperature, thermal stability, and carbon yield of the 3D-printed resins were evaluated by thermogravimetric analysis (TGA) coupled with differential scanning calorimetry (DSC) using an STA 449 F3 Jupiter® from Netzsch. Approximately 10 mg of photopolymerized resin was loaded into a platinum crucible and heated from room temperature to

800 °C at 10 °C·min^{-1} under argon flow. The argon flow was then replaced by air to deduce the resulting ash content.

Thermal oxidation of carbon samples was studied by thermogravimetric analysis (TGA) under non-isothermal conditions. About 11 mg of sample was placed in an alumina crucible, and the temperature was increased at a constant heating rate β of either 5, 10, 15 or 20 °C·min^{-1}, from room temperature to 1200 °C, under a constant synthetic air flow of 50 mL·min^{-1}. The kinetic parameters were calculated by the Kissinger-Akahira-Sunose (KAS) isoconversional method.

To this end, conversion-temperature curves were calculated from the TGA experimental results according to Equation (3) where m_0 and m_∞ are the initial and final masses of the sample, respectively, ignoring the initial mass loss at temperatures below 150 °C, attributed to evaporation of moisture:

$$\alpha = \frac{m_0 - m(T)}{m_0 - m_\infty} \quad (1)$$

where α (dimensionless) is the conversion, and $m(T)$ is the mass of the sample at temperature T. The apparent reaction rate, $d\alpha/dt = \beta\, d\alpha/dT$, was then calculated as the differential of the conversion degree with respect to time t.

Structure and textural properties of carbon materials

Scanning Electron Microscopy (SEM) was performed with a Zeiss GeminiSEM 500 microscope using secondary electrons accelerated under 5 kV to observe the general morphology of the samples.

Raman spectra were recorded with a Horiba XploRa Raman apparatus equipped with a 50× long-range objective. The spectra were obtained using a 1200 lines per mm holographic grating

with a circularly polarized laser (wavelength of 638 nm, filtered at 10% of its maximum energy to avoid heating of the samples, accumulation of 2 spectra for each material) in the Raman shift range of 200 to 3800 cm^{-1}.

The bulk density of the carbon architectures, ρ_b ($g \cdot cm^{-3}$), defined as the mass of the materials divided by their total volume, was simply obtained by weighing samples of known dimensions and calculating the average. The skeletal density, ρ_s ($g \cdot cm^{-3}$), was determined by helium pycnometry using an automatic Accupyc II 1340 (Micromeritics) apparatus by averaging 30 measurements for each carbon sample. Each sample was ground in a mortar to avoid neglecting a possible closed porosity fraction and then dried at 105 °C for several hours before measurement. The total porosity Φ (dimensionless) was calculated according to Equation (1) from the experimental values of the bulk and skeletal densities.

$$\Phi = 1 - \frac{\rho_b}{\rho_s} \quad (2)$$

Mercury intrusion was performed using a Micromeretics AutoPore IV 9500 apparatus. The experiments were conducted at two different pressure ranges, from 0.001 to 0.24 MPa and from 0.24 to 414 MPa. The inlet pore diameter, D (m), was calculated by application of the Washburn equation:

$$D = -\frac{4\gamma \cos\varphi}{P} \quad (3)$$

where γ (0.485 $J \cdot m^{-2}$) is the surface tension of mercury, φ (140°) is the contact angle between mercury and carbon, and P (Pa) is the intrusion pressure.

N_2 adsorption experiments at -196°C were carried out with a Micromeritics ASAP 2020 automatic adsorption apparatus. Samples (~ 1 g) were degassed under vacuum before analysis for

196 at least 48h at 110 °C. The Brunauer-Emmett-Teller [31,32] (BET) method was applied to N_2
197 isotherms to obtain the BET area, A_{BET} ($m^2 \cdot g^{-1}$). The pore size distributions were determined
198 from the N_2 isotherms using the NLDFT model available in the SAIEUS software (Micromeritics
199 [33]). The model was used to calculate surface area, S_{NLDFT} ($m^2 \cdot g^{-1}$), total pore volume V_{tot} ($cm^3 \cdot g^{-1}$),
200 ultramicropore volume $V_{u\mu}$ ($cm^3 \cdot g^{-1}$) (pore size $w < 0.7$ nm), supermicropore volume $V_{s\mu}$ ($cm^3 \cdot g^{-1}$)
201 ($0.7 < w < 2$nm), and mesopore volume V_{meso} ($cm^3 \cdot g^{-1}$) = V_{tot} - $V_{s\mu}$ - $V_{u\mu}$.

202

203 *Physical properties*

204 The electrical conductivity σ ($S \cdot cm^{-1}$) was measured by the four-point method using a Keithley
205 6430 source-measure unit and then calculated according to:

206 $$\sigma = \frac{2\,I}{(|V^+| + |V^-|)} \frac{L}{S} \qquad (4)$$

207 where V^+ and V^- are the voltage values (V) measured with the current I (A) flowing in one
208 direction and then in the other, so as to correct the existing weak thermoelectric effect. S (cm^2) is
209 the cross-sectional area, and L (cm) is the distance between the two opposite sides on which the
210 electrical contacts were placed. The electrical conductivity of the carbon skeleton, σ_s ($S \cdot cm^{-1}$)
211 was then estimated from Equation 5), assuming that these porous carbons behave like rigid open-
212 cell foams with node effect:

213 $$\sigma_s = \frac{3\sigma}{\left[(1-\Phi)+2(1-\Phi)^{\frac{3}{2}}\right]} \qquad (5)$$

214 The mechanical properties of the carbons were finally obtained in triplicate at a constant
215 compression rate using a universal testing machine (Instron 5944) equipped with a 2kN load cell.

The samples were compressed along their printing direction (*i.e.*, orthogonal to the successive layers) after bonding to PMMA plates with a very thin layer of epoxy glue. The deformation (mm) and applied force (N) were continuously recorded. The strain (%) and stress (MPa) were obtained from the recorded data and the known dimensions of the samples. Finally, the Young's modulus, defined as the slope of the initial linear part of the compression curve presenting the steepest slope, and the compressive strength at break were estimated from the stress-strain curves.

RESULTS AND DISCUSSION

Characterization of acylated vanillin and tannin

The FT-IR spectra of vanillin methacrylate (Vm) and tannin methacrylate (Tm) are shown in Figure 2a. The disappearance of the 3300 cm^{-1} band and the appearance of the 1740 cm^{-1} and 950 cm^{-1} bands in the spectrum of vanillin-methacrylate indicates the consumption of hydroxyl groups attached to the aromatic rings and the reaction between the phenolic group and the methacrylate anhydride (see again Figure 1). Similarly, in the spectrum of the modified tannin, the appearance of C=O and C=C bands indicates that the grafting reaction suggested in Figure 1 has taken place. However, the intensity of the band at 3300 cm^{-1} was only partially reduced, indicating that some hydroxyl groups were unreacted or not accessible. Similar results have also been demonstrated in the literature by solid-state NMR.[34,35]

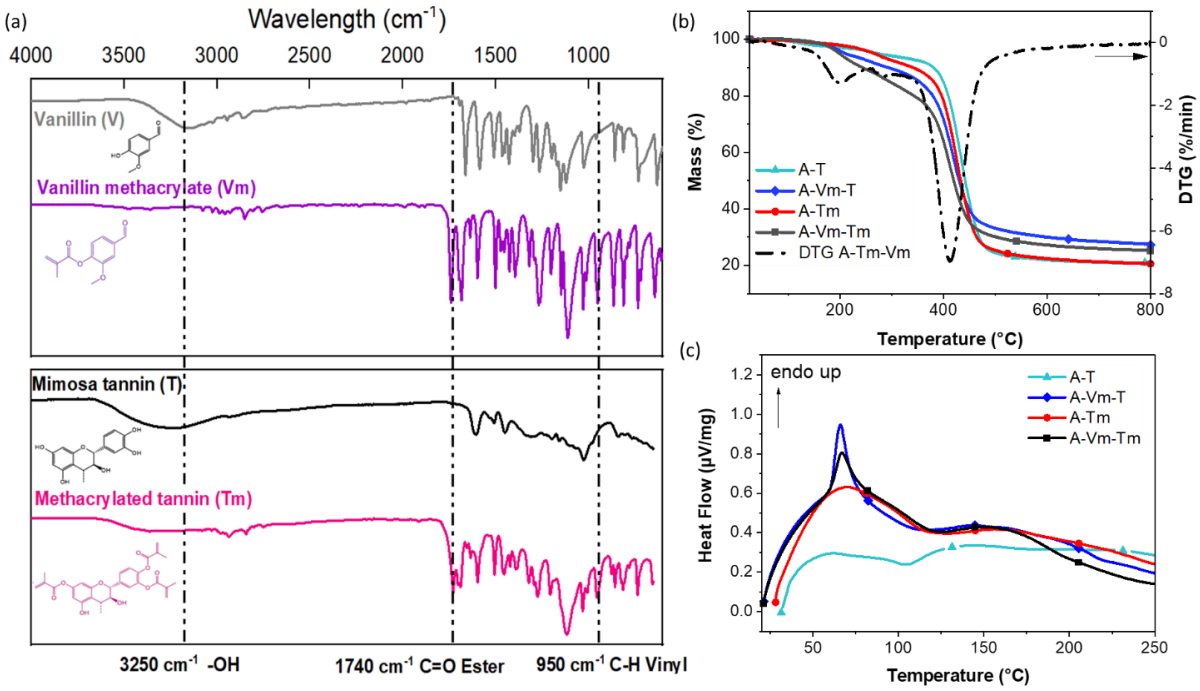

Figure 2. (a) FT-IR spectra of vanillin, mimosa tannin, and their respective methacrylate derivatives; (b) TGA (mass loss) and (c) DSC curves, under argon flow, of A-T, A-Vm-T, A-Tm, and A-Vm-Tm resins.

Thermal behaviour and carbon yield

Figure 2b and 2c shows the TGA and DSC curves of the different photocurable resins (A-T, A-Vm-T, A-Tm, and A-Vm-Tm). For all formulations, two regions of significant mass loss were identified (Figure 2b) The first region, located between 30 and 310 °C, with a DTG peak around 200 °C, corresponds to the release of water molecules resulting from the intramolecular condensation of tannin hydroxyl groups and the beginning of the degradation of free acrylate chains [36]. The second region, between 310 and 680 °C, corresponds to the decomposition of the rigid segments and the formation of carbonaceous material.

As expected, the addition of vanillin significantly increased the final carbon yield at 800 °C, from 20.8 % for acrylate-tannin resins to values of 27.6 % and 25.4 % for A-Vm-T and A-Vm-Tm, respectively (Figure 2b). However, the integration of tannin-methacrylate into the photoreactive resin did not lead to a significant improvement in carbon yield (20.7 %). In addition, for all samples, the ash content remained below 0.5 wt.%.

The DSC thermograms, obtained immediately after curing, exhibit clear endothermic peaks around 70 °C, which, despite the mass loss not clearly observed in the TGA graphs, can be attributed to the evaporation of moisture from the samples in the semi-open DSC crucible. Due to the presence of acrylate moieties on vanillin or mimosa tannin, the glass transition temperature T_g of the final resin was found to be 130, 142, and 139 °C for A-Vm-T, A-Tm, and A-Vm-Tm, respectively (see Figure 2c and Figure S1). These values, higher than those measured for acrylate-tannin resins (115 °C) [13], indicate a significant increase in polymer rigidity likely induced by limited rotation of aromatic moieties [25]. The high T_g values suggest that Vm and Tm monomers have been incorporated into the acrylate polymer chains, which led to an increased cross-linking density, thus allowing for better stabilization of the architecture during heat treatment.[37]

Morphology and composition

In order to illustrate the freedom of geometry and the definition of 3D printed carbon architectures, solid cubes, 2×2 Kelvin cell architectures and structured cylinders were printed from 30 µm-thick layers. While the carbon cubes obtained after pyrolysis of the acrylate-tannin resin showed some cracks, matte black structures with slight deformation but no cracks were obtained from A-Vm-T, A-Tm (see Figure 3) and A-Tm-Vm resins. Nevertheless, the thermal stabilization and increase in carbon yield upon pyrolysis observed with the addition of chemically

modified bio-based precursors were found to have no particular effect on structure shrinkage, with values of about 25 % in each direction, similar to those observed for carbon based on acrylate-tannin [13].

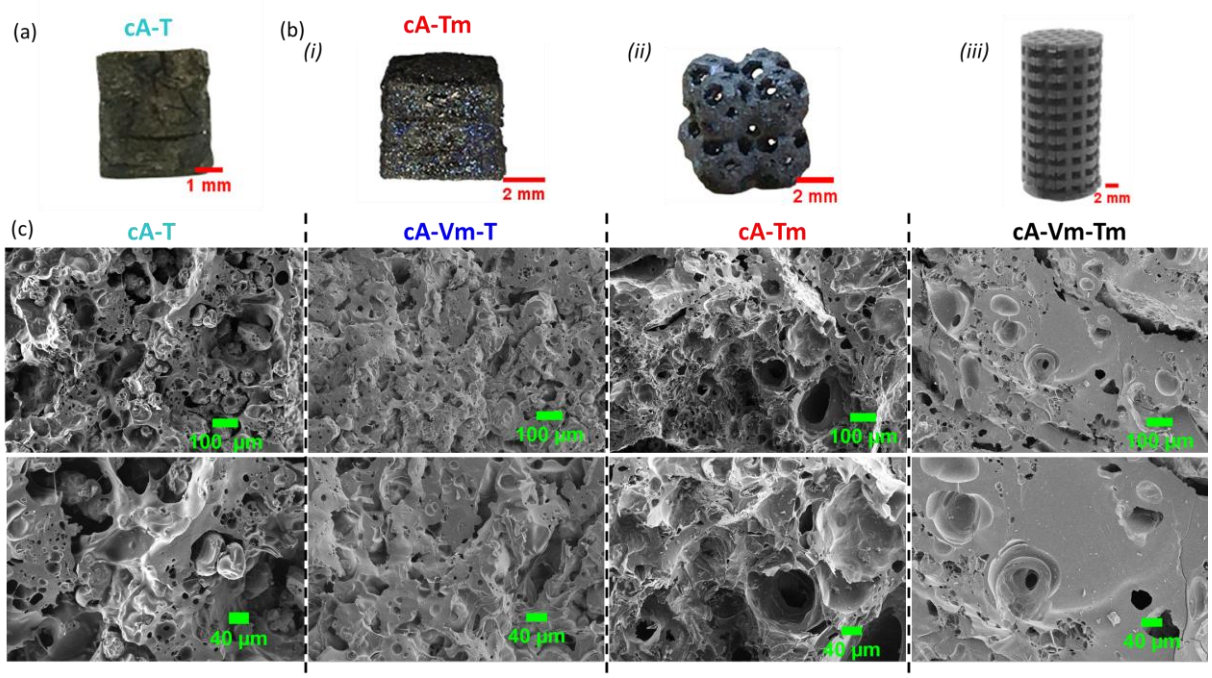

Figure 3. Examples of carbon geometries 3D printed by SLA: (a) Solid cube printed from A-T resin. (b) samples printed from A-Tm resin and pyrolyzed at 900°C: (i) solid cube, (ii) Kelvin cells and (iii) cylindrical architecture; samples produced from the other formulations (not shown) do not differ visibly from these. (c) SEM images of a fractured areas of cA-T, cA-Vm-T, cA-Tm and cA-Vm-Tm samples obtained from 3D-printed cubes; scale bar: 100 µm (top row) and 40 µm (bottom row).

SEM images of fractured carbon structures (Figure 3e) revealed porosities and pore morphologies with marked differences between samples. The tannin- and tannin-methacrylate-derived carbons show significant and rather homogeneous internal porosity with many narrow pores in the presence of a few larger round pores. With the addition of vanillin-methacrylate

monomers to the photosensitive resin, the inner porosity of the derived carbons is particularly reduced and appears more inhomogeneous with the presence of only a few large oval pores.

Table S1 presents the bulk chemical composition of the carbons printed in 3D from the different resins. Sulfur (S) was not detected, hydrogen (H) and nitrogen (N) contents turned out to be very low, whereas oxygen (O) was found in significant amounts in the carbon structure (around 4.5 wt.%). These observations are in agreement with the general composition of other carbons derived from mimosa tannin [38,39]. Furthermore, the addition of acrylate moieties on tannin and the addition of Vm in the acrylate-tannin resin have increased the oxygen and nitrogen contents in the carbon compared to acrylate-tannin-based carbon. A similar trend of oxygen increase was also observed for the surface chemistry determined by XPS (Table S2).

Figure S2a shows the XPS spectra corresponding to the C1s band of carbon, for the different 3D-printed carbon materials. The relative contribution of the various corresponding functional groups is given in Table S3 of the Supporting Information. In all samples, the main contributions to the C1s peak are graphite-type (C_I, 284.4 eV) as represented by a typical asymmetric line and a band assigned to C-OH functional groups (C_{II}, 285.5 eV). The contribution of C=O functional groups (C_{III}, 287.5 eV) is relatively low for all materials, but even more so for cA-T, which on the other hand shows a larger O=C-OH contribution (C_{IV}, 289.1 eV). Finally, the contribution of satellite bonds remains of the same order of magnitude for all samples.

The relative contributions of the various O moieties to the O1s band, shown for the different 3D-printed carbons in Figure S2b, hightlight notable differences in the surface chemistries. The dominant contribution of phenol hydroxyl groups (O_{II}, 532.7 eV) for samples cA-Tm, cA-Vm-Tm and cA-Vm-Tm is in good agreement with the phenolic nature of the bio-based carbon precursors, while the dominant contribution of quinone groups (O_I, 531.4 eV) in sample cA-T

suggests the oxidation of phenolic tannin groups during processing.[40] These results show that the chemical modification of tannin affected the surface chemistry of the resulting carbons.

Textural properties

The bulk density of the 3D-printed carbons was particularly influenced by the formulations (see Table 2). With bulk densities ranging from 0.63 to 0.74 $g \cdot cm^{-3}$, the materials obtained from resins containing vanillin methacrylate were denser than their counterparts based on tannin (0.41 $g \cdot cm^{-3}$) or acetylated tannin (0.49 $g \cdot cm^{-3}$).

Table 2. Pore texture parameters of 3D-printed carbon structures depending on their initial formulation.

Sample	cA-T	cA-Vm-T	cA-Tm	cA-Vm-Tm
ρ_b ($g \cdot cm^{-3}$)	0.41	0.63	0.49	0.74
ρ_s ($g \cdot cm^{-3}$)	1.85	1.70	1.85	1.66
Φ (%)	78	63	73	55
A_{BET} ($m^2 \cdot g^{-1}$)	355	54	28	≈3
V_{tot} ($cm^3 \cdot g^{-1}$)	0.22	0.024	0.01	0.004
V_{meso} ($cm^3 \cdot g^{-1}$)	0	0.0028	0	0.0035
V_{mic} ($cm^3 \cdot g^{-1}$)	0.22	0.021	0.01	0.0004

This difference can be explained by the significant increase in carbon yield due to a reduced mass loss (due the limited depolymerization of the polymers during pyrolysis) for a similar linear shrinkage. The exchange of tannin with tannin methacrylate in the photocurable formulation led to carbon architecture with the same skeletal density (1.85 $g \cdot cm^{-3}$) and a slightly reduced porosity

with values decreasing from 78% to 73%. In comparison, the addition of the vanillin methacrylate monomer led to a significant reduction in skeletal density (from 1.85 to 1.66 g·cm^{-3}) and total porosity, with values decreasing from 78% to 55%. These measurements confirmed the SEM observations.

The textural properties of the materials and the influence of the resin formulation on the surface area after pyrolysis was investigated by N_2 adsorption-desorption isotherms at 77 K (Figure 4) and are summarized in Table 2.

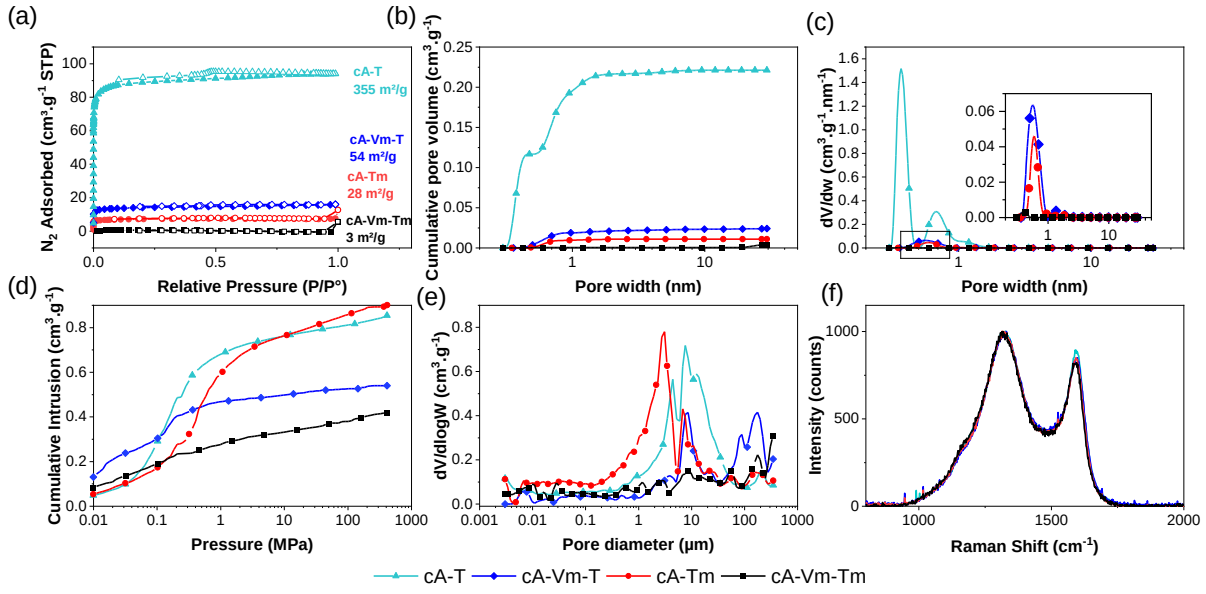

Figure 4. Textural properties of 3D-printed carbons cA-T, cA-Tm, cA-Vm-T and cA-Vm-Tm: (a) Nitrogen adsorption (full symbols) – desorption (empty symbols) isotherms and corresponding: (b) cumulative pore volumes, (c) pore size distributions calculated by application of the NLDFT model, with a zoom on the boxed area of the graph. Results of mercury porosimetry : (d) raw intrusion curves, and (e) corresponding pore size distributions. (f) Raman spectra, obtained at 638 nm, of 3D-printed carbon structures for the different acrylate/vanillin/tannin or tannin methacrylate formulations.

The outgassing of the samples was particularly long, indicating extremely narrow porosity. Thus as expected, Figure 4a shows type Ia nitrogen isotherms with hysteresis at low pressure, typical of microporous materials with predominantly narrow pores, which might prevent N_2 acess. The amount of absorbed nitrogen decreased with the density of the material, and thus the A_{BET} values ranged from 300 to 3 $m^2 \cdot g^{-1}$. The total pore volumes, V_{tot}, were extremely low, between 0.22 and 0.004 $cm^3 \cdot g^{-1}$ and were mainly composed of ultramicropores. Although in almost neglible amounts, cA-Vm-T and cA-Vm-Tm showed some mesopores with volumes of 0.0028 $cm^3 \cdot g^{-1}$ and 0.0035 $cm^3 \cdot g^{-1}$, respectively (see Table 2 and Figure 4b). Micropores are formed mainly during carbonization by volatilization of small molecules such as water and CO_2, and the increase in pore and micropores volumes for carbon derived from tannin resins may be related to the greater mass loss from these resins during pyrolysis.

Finally, as can be seen in Figure 4c, cA-Tm and cA-Vm-T materials had similar pore size distributions with a narrow and well-defined peak around 0.6 nm, whereas the cA-T and cA-Vm-Tm carbons exhibited smaller pore sizes (0.4 nm).

Overall, the low surface area of such materials can be interesting for the development of sodium-ion batteries such as those developped by Beda *et al.* [41,42] or Tonnoir *et al.* [43] (see the comparison of textural properties in Table S4).

Raw and differential mercury intrusion of the different porous carbons is shown inFigure **4**d and 4e. The corresponding curves confirm that most of the pore volume could be attributed to large pores, as observed in the SEM images, in which gas adsorption is negligibly small. The addition of functionalized vanillin to the initial acrylate-tannin resin reduced the overall porosity, with a median pore value of about 10 µm. In contrast, the chemical modification of tannin was found to shift the median pore diameter (calculated with Equation 2) to lower values, with a

distribution centered on a diameter of 3 µm.The average pore diameters were significantly lower than those reported for 3D-printed carbon based on acrylate-tannin resin [13].

The Raman spectra (Figure 4f) are typical of highly disordered carbons, as expected from the precursors used. Indeed, the D band, whose maximum is around 1320 cm^{-1}, is very broad with a shoulder around 1160 cm^{-1}, and the G band, centered around 1590 cm^{-1}, is just a little narrower. The spectra are very similar from one formulation to the other, but when moving from the cA-T sample to the cA-Vm-Tm sample, the D/G intensity ratio increased from 1.1 to 1.2. Considering the well-known non-graphitizable character of this kind of bio-based carbon [38,39], this evolution corresponds to a slight increase in the size of coherent domains L_c, thus a little less disorder in the stacking axis of the graphene-like nanosheets.

Reactivity to hot oxidation

Figure 5a and Figure S3 shows the conversion and reaction rate curves as a function of temperature for the different carbon samples. As can be seen, the curves systematically shift to higher temperatures and higher oxidation rate with increasing heating rate, which is typical of solid-state oxidation. Moreover, at higher heating rates (15 °C·min^{-1} and 20 °C·min^{-1}), the reaction rate curves of cA-T and cA-Tm show an almost bimodal character, suggesting a change in the mechanism that controls oxidation. Seifi *et al.* [44] thus suggested that, at high temperatures, the overall oxidation rate is controlled by pore diffusion, an effect that becomes even more significant at high heating rates due to excess gas generated at the corresponding time scale. Thus, the oxidation reactions of the samples with the highest porosity, cA-T and cA-Tm, are less influenced by diffusional limitation as confirmed by the slight decrease of the oxidation rate at 650 °C, followed by a plateau until full conversion.

In Figure 5b, 5c and Figure S4, the reaction rates of the different samples at the same heating rates are compared to better understand the effect of carbon formulations and textural properties on the oxidation behavior of the 3D-printed architectures. As can be seen, regarless of heating rate, the temperature range in which mass loss occurs shifts to higher values from cA-T to cA-Vm-Tm. As expected, cA-T is the material of maximum oxidation rate due to its larger surface area, confirming that oxidation is mainly controlled by the textural properties of the carbon structures [44]. Thus, due to their lower porosity and surface area, the oxidation resistance of the 3D-printed porous carbon was significantly improved by adding vanillin methacrylate and tannin methacrylate into the photoreactive resin. It is indeed these modified monomers that changed the textural properties and density of the resulting carbonaceous materials and, by leading to samples of higher density - thus much lower porosity - and significantly lower specific surface area, they made it possible to obtain carbons that oxidize more slowly, and at higher temperatures.

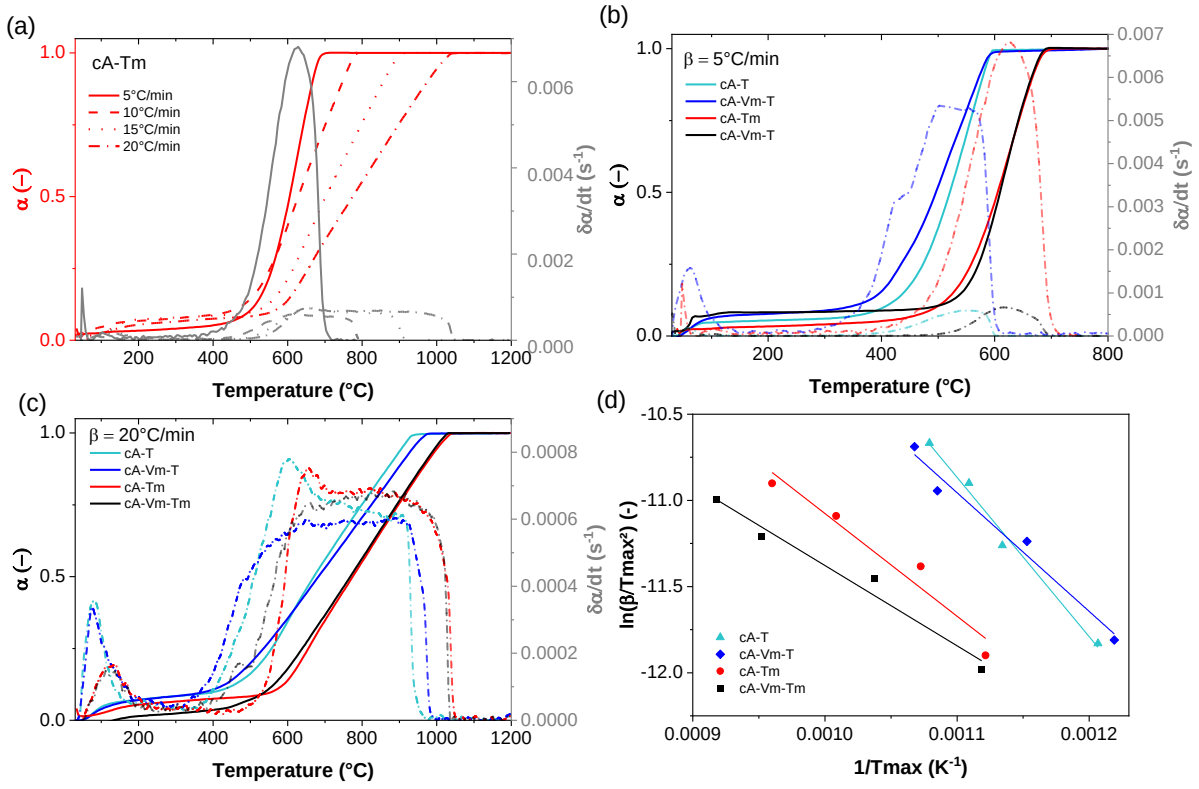

Figure 5. (a) Conversion and reaction rate curves versus temperature for sample cA-Tm. Conversion and reaction rate curves of the different 3D-printed carbon samples at heating rates of: (b) 5 C·min^{-1} and (c) 20 °C·min^{-1}. (d) isoconversion plot used to calculate the apparent activation energy at the maximum mass loss rate by the KAS method.

The KAS method, a reliable integral method, was chosen for isoconversional calculation of the activation energy. The apparent reaction rate dα/dt is such that:

$$\beta \frac{\mathrm{d}\alpha}{\mathrm{d}t} = A \exp\left(-\frac{E_\mathrm{a}}{\mathrm{R}T}\right) f(\alpha) \qquad (6)$$

where t is the time, β is the heating rate, A is the pre-exponential factor, E_a is the apparent activation energy, R is the universal gas constant (8.314 J·mol^{-1}·K^{-1}), T is the absolute temperature and $f(\alpha)$ is the differential conversion function.

According to Equation (6), the activation energy is obtained from the slope of the linear fit resulting from plotting $\ln(\beta/T_{max}^2)$ versus $1/T_{max}$, with T_{max} the temperature at which the conversion rate is maximal (see Figure 5d). The obtained values of E_a (see Table S5) decreased from 76 kJ·mol^{-1} for cA-T to 38 kJ·mol^{-1} for cA-Vm-Tm, and remained, as expected, lower than values reported for activated carbon (between 105 and 340 kJ·mol^{-1}) having much higher surface areas [45].

The results of the isoconversional method confirmed the determining role of textural properties in the overall kinetics of the oxidation reaction. Thus, the 3D-printed structures derived from cA-Tm, cA-Vm-T, and cA-Vm-Tm can be used in an oxidizing environment at higher temperatures than the cA-T structures.

This high oxidation resistance coupled with their textural properties (broad macropores) suggests that the 3D-printed bio-based carbon monoliths could be interesting catalyst supports for

the preferential oxidation of carbon monoxide (CO-PrOx) such as those demonstrated by Chaparro-Garnica *et al.*[46–48]. The monoliths presented in this work are even more versatile, allowing for greater freedom of architecture, a wide range of porosity and a reduction in the number of steps to obtain the carbon support.

Physical properties of printed carbon structures

The stress-strain curves of the 3D-printed carbon materials are given in Figure 6a and suggest a typical elastic-brittle behavior followed by a progressive densification of the material at strain over 20%. The Young's modulus, ranging from 301.7 to 387 MPa, and the compressive strength, with values between 6.7 and 8.3 MPa, increased linearly with the bulk density (see Figure 6 and Table S6). Due to the reduction in porosity with the addition of Vm, the carbon becomes more brittle and a reduction of strain at break can be observed, from 3.1 for cA-Tm to 2.7% for cA-Vm-Tm carbon. As expected, due to a denser structure, the mechanical properties of the 3D-printed carbons studied in this work were superior to those of previously studied carbons based on acrylate-tannin resin.[13,14] In the broader context of carbon monoliths, the 3D-printed carbons derived from Vm and Tm precursors exhibit similar or most of the time better mechanical properties than other stereolithographically printed petroleum-derived carbons, DIW-printed carbons or carbon foams and gels with densities in the range 0.4 to 0.7 $g \cdot cm^{-3}$.[6,13,14,49–52] These results may be interpreted in terms of thick matrix containing fewer and fewer pores, which leads to much stiffer carbon materials than typical carbon foams, which typically have much thinner struts. It is indeed known that for a porous material of constant density, larger cells lead to lower compressive strengths.[53]

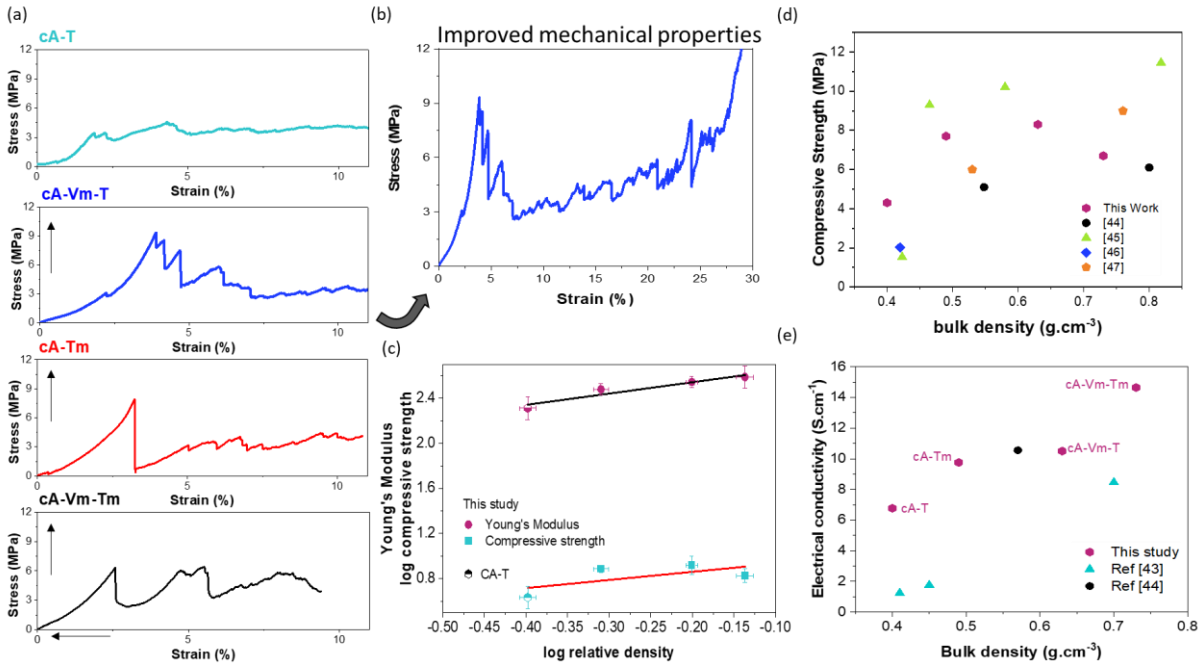

Figure 6. (a) Strain-stress characteristics of the 3D-printed carbon structures submitted to uniaxial quasi-static compression. (b) Strain-stress curve of the cA-Vm-T sample showing densification of the material at strain above 20%. (c) Compressive strength and Young's modulus as a function relative density of the different 3D-printed carbons, in double-log scale; (d) Compressive strength as a function of bulk density for the 3D-printed carbons presented in this work, DIW-printed carbons,[49] carbon gels and carbon foams from the litterature[50–52]; and (e) electrical conductivity of the 3D-printed carbons as a function of bulk density, compared with carbon gels derived from tannin[54] and wood bioachar[55].

The electrical conductivity of carbon structures varies considerably with the texture and relative density of the material. Thus, as expected, the electrical conductivity of 3D-printed carbons increased almost linearly with bulk density, with values ranging from 6.77 to 14.65 $S \cdot cm^{-1}$ (Figure 6e and Table S7). The electrical conductivity of the 3D-printed carbons was found

to be higher than that of biochar and carbon gels of similar densities, with values between 1.24 and 10 $S \cdot cm^{-1}$ (See Figure 6e).[54,55]

Since the different, highly disordered, 3D-printed carbons are derived from the same raw precursors, the electrical conductivity of the skeleton is assumed to remain of the same order of magnitude. Indeed, Table S7 shows values between 38 and 54 $S \cdot cm^{-1}$, which is similar to other 3D-printed carbons based on acrylate-tannin resins (between 43 and 59 $S \cdot cm^{-1}$), wood biochar (between 11 and 33 $S \cdot cm^{-1}$)[55,56] and to that of glassy carbon in general, for which values from 11 $S \cdot cm^{-1}$ [57] to 70 $S \cdot cm^{-1}$ [58] have been reported.

CONCLUSION

New 3D-printed porous carbon architectures with improved mechanical properties and oxidation resistance were prepared by blending chemically modified vanillin monomer and tannin precursor into a photocurable resin designed for stereolithography.

The functionalization of vanillin and tannin with methacrylate allowed their integration into the acrylate polymer network, improved thermal stabilization, and reduced depolymerization of free chains, thereby increasing the carbon yield up to 27 %. Due to a reduced overall porosity (between 55 and 70 %) and the low surface area of these new carbon materials obtained after pyrolysis at 900 °C, the thermo-oxidation kinetics were considerably lower than that of acrylate-tannin derived carbon, demonstrating the ability to use the 3D-printed architectures under extreme oxidation conditions at relatively high temperatures (up to about 500 °C with reduced mass loss).

In addition, these materials, whose density (between 0.4 and 0.7) depends on the formulation of the photosensitive resin, exhibited outstanding performances in terms of mechanical behavior, with Young's modulus values above 310 MPa, and in terms of electrical conductivity when compared with carbon foam of similar densities.

Therefore, this study has provided an efficient, low-cost, and sustainable approach to prepare complex carbon architectures with a great freedom of geometry and properties that can be used in a broad range of applications, among them sodium-ion batteries (due to the non-graphitizable nature of this carbon and its very low specific surface area of the material) and catalyst supports (thanks to a wide macroporosity and a high thermal and oxidative stability).

ASSOCIATED CONTENT

Supporting information: Additional experimental details and results including data and figures related to elemental analysis, determination of glass transition temperature and physical properties (oxidation, mechanical and electrical properties) of the different 3D-printed carbons. This material is available free of charge via the Internet at http://pubs.acs.org.

AUTHOR INFORMATION

* Corresponding author. Tel: + 33 372 74 96 14. E-mail address: alain.celzard@univ-lorraine.fr (A. Celzard)

Funding Sources

This study was partially funded by ERDF [TALiSMAN project (2019-000214)].

ACKNOWLEDGEMENT

Pauline Blyweert gratefully acknowledges the support of the French Ministry of Higher Education and the Grand-Est region for her PhD grant, resulting in the work presented herein. The authors wish to thank Arkema and Solvay for providing the acrylates monomers and the vanillin used in this work, and M.T. Izquierdo for performing the XPS experiments and for providing us with the corresponding data.

REFERENCES

(1) Blyweert, P.; Nicolas, V.; Fierro, V.; Celzard, A. 3D Printing of Carbon-Based Materials : A Review. *Carbon* **2021**, *183*, 449–485. https://doi.org/10.1016/j.carbon.2021.07.036.

(2) Jorge, A. B.; Jervis, R.; Periasamy, A. P.; Qiao, M.; Feng, J.; Tran, L. N.; Titirici, M.-M. 3D Carbon Materials for Efficient Oxygen and Hydrogen Electrocatalysis. *Advanced Energy Materials* **2020**, *10* (11), 1902494. https://doi.org/10.1002/aenm.201902494.

(3) Pagac, M.; Hajnys, J.; Ma, Q.-P.; Jancar, L.; Jansa, J.; Stefek, P.; Mesicek, J. A Review of Vat Photopolymerization Technology: Materials, Applications, Challenges, and Future Trends of 3D Printing. *Polymers* **2021**, *13* (4), 598. https://doi.org/10.3390/polym13040598.

(4) Bagheri, A.; Jin, J. Photopolymerization in 3D Printing. *ACS Appl. Polym. Mater.* **2019**, *1* (4), 593–611. https://doi.org/10.1021/acsapm.8b00165.

(5) Bian, B.; Shi, D.; Cai, X.; Hu, M.; Guo, Q.; Zhang, C.; Wang, Q.; Sun, A. X.; Yang, J. 3D Printed Porous Carbon Anode for Enhanced Power Generation in Microbial Fuel Cell. *Nano Energy* **2018**, *44*, 174–180. https://doi.org/10.1016/j.nanoen.2017.11.070.

(6) Steldinger, H.; Esposito, A.; Brunnengräber, K.; Gläsel, J.; Etzold, B. J. M. Activated Carbon in the Third Dimension—3D Printing of a Tuned Porous Carbon. *Adv. Sci.* **2019**, *6* (19), 1901340. https://doi.org/10.1002/advs.201901340.

(7) Wang, P.; Zhang, H.; Wang, H.; Li, D.; Xuan, J.; Zhang, L. Hybrid Manufacturing of 3D Hierarchical Porous Carbons for Electrochemical Storage. *Adv. Mater. Technol.* **2020**, *5* (6), 1901030. https://doi.org/10.1002/admt.201901030.

(8) Rezaei, B.; Pan, J. Y.; Gundlach, C.; Keller, S. S. Highly Structured 3D Pyrolytic Carbon Electrodes Derived from Additive Manufacturing Technology. *Materials & Design* **2020**, *193*, 108834. https://doi.org/10.1016/j.matdes.2020.108834.

(9) Narita, K.; Citrin, M. A.; Yang, H.; Xia, X.; Greer, J. R. 3D Architected Carbon Electrodes for Energy Storage. *Advanced Energy Materials* **2021**, *11* (5), 2002637. https://doi.org/10.1002/aenm.202002637.

(10) Zafanelli, L. F. A. S.; Henrique, A.; Steldinger, H.; Diaz de Tuesta, J. L.; Gläsel, J.; Rodrigues, A. E.; Gomes, H. T.; Etzold, B. J. M.; Silva, J. A. C. 3D-Printed Activated Carbon for Post-Combustion CO2 Capture. *Microporous and Mesoporous Materials* **2022**, *335*, 111818. https://doi.org/10.1016/j.micromeso.2022.111818.

(11) Szczurek, A.; Ortona, A.; Ferrari, L.; Rezaei, E.; Medjahdi, G.; Fierro, V.; Bychanok, D.; Kuzhir, P.; Celzard, A. Carbon Periodic Cellular Architectures. *Carbon* **2015**, *88*, 70–85. https://doi.org/10.1016/j.carbon.2015.02.069.

(12) Chen, X.; Zhao, G.; Wu, Y.; Huang, Y.; Liu, Y.; He, J.; Wang, L.; Lian, Q.; Li, D. Cellular Carbon Microstructures Developed by Using Stereolithography. *Carbon* **2017**, *123*, 34–44. https://doi.org/10.1016/j.carbon.2017.07.043.
(13) Blyweert, P.; Nicolas, V.; Macutkevic, J.; Fierro, V.; Celzard, A. Tannin-Based Resins for 3D Printing of Porous Carbon Architectures. *ACS Sustainable Chem. Eng.* **2022**. https://doi.org/10.1021/acssuschemeng.2c01686.
(14) Blyweert, P.; Nicolas, V.; Fierro, V.; Celzard, A. Experimental Design Optimisation of Tannin-Acrylate Photocurable Resins for 3D Printing of Biobased Porous Carbon Architectures. *Molecules* **2022**. https://doi.org/10.3390/molecules27072091.
(15) Zakeri, S.; Vippola, M.; Levänen, E. A Comprehensive Review of the Photopolymerization of Ceramic Resins Used in Stereolithography. *Additive Manufacturing* **2020**, *35*, 101177. https://doi.org/10.1016/j.addma.2020.101177.
(16) Zhang, C.; Madbouly, S. A.; Kessler, M. R. Renewable Polymers Prepared from Vanillin and Its Derivatives. *Macromolecular Chemistry and Physics* **2015**, *216* (17), 1816–1822. https://doi.org/10.1002/macp.201500194.
(17) Stanzione, J. F.; Giangiulio, P. A.; Sadler, J. M.; La Scala, J. J.; Wool, R. P. Lignin-Based Bio-Oil Mimic as Biobased Resin for Composite Applications. *ACS Sustainable Chem. Eng.* **2013**, *1* (4), 419–426. https://doi.org/10.1021/sc3001492.
(18) Voet, V. S. D.; Strating, T.; Schnelting, G. H. M.; Dijkstra, P.; Tietema, M.; Xu, J.; Woortman, A. J. J.; Loos, K.; Jager, J.; Folkersma, R. Biobased Acrylate Photocurable Resin Formulation for Stereolithography 3D Printing. *ACS Omega* **2018**, *3* (2), 1403–1408. https://doi.org/10.1021/acsomega.7b01648.
(19) Ding, R.; Du, Y.; Goncalves, R. B.; Francis, L. F.; Reineke, T. M. Sustainable near UV-Curable Acrylates Based on Natural Phenolics for Stereolithography 3D Printing. *Polym. Chem.* **2019**, *10* (9), 1067–1077. https://doi.org/10.1039/C8PY01652F.
(20) Bassett, A. W.; Honnig, A. E.; Breyta, C. M.; Dunn, I. C.; La Scala, J. J.; Stanzione, J. F. Vanillin-Based Resin for Additive Manufacturing. *ACS Sustainable Chem. Eng.* **2020**, *8* (14), 5626–5635. https://doi.org/10.1021/acssuschemeng.0c00159.
(21) Anastas, P.; Eghbali, N. Green Chemistry: Principles and Practice. *Chemical Society Reviews* **2010**, *39* (1), 301–312. https://doi.org/10.1039/B918763B.
(22) Navaruckiene, A.; Skliutas, E.; Kasetaite, S.; Rekštytė, S.; Raudoniene, V.; Bridziuviene, D.; Malinauskas, M.; Ostrauskaite, J. Vanillin Acrylate-Based Resins for Optical 3D Printing. *Polymers* **2020**, *12* (2), 397. https://doi.org/10.3390/polym12020397.
(23) Arbenz, A.; Avérous, L. Chemical Modification of Tannins to Elaborate Aromatic Biobased Macromolecular Architectures. *Green Chem.* **2015**, *17* (5), 2626–2646. https://doi.org/10.1039/C5GC00282F.
(24) Liao, J.; Brosse, N.; Pizzi, A.; Hoppe, S.; Zhou, X.; Du, G. Characterization and 3D Printability of Poly (Lactic Acid)/Acetylated Tannin Composites. *Industrial Crops and Products* **2020**, *149*, 112320. https://doi.org/10.1016/j.indcrop.2020.112320.
(25) Holmberg, A. L.; Reno, K. H.; Nguyen, N. A.; Wool, R. P.; Epps, T. H. Syringyl Methacrylate, a Hardwood Lignin-Based Monomer for High-Tg Polymeric Materials. *ACS Macro Lett* **2016**, *5* (5), 574–578. https://doi.org/10.1021/acsmacrolett.6b00270.
(26) Sutton, J. T.; Rajan, K.; Harper, D. P.; Chmely, S. C. Lignin-Containing Photoactive Resins for 3D Printing by Stereolithography. *ACS Appl. Mater. Interfaces* **2018**, *10* (42), 36456–36463. https://doi.org/10.1021/acsami.8b13031.
(27) Sutton, J. T.; Rajan, K.; Harper, D. P.; Chmely, S. C. Improving UV Curing in Organosolv Lignin-Containing Photopolymers for Stereolithography by Reduction and Acylation. *Polymers* **2021**, *13* (20), 3473. https://doi.org/10.3390/polym13203473.
(28) Zhang, S.; Li, M.; Hao, N.; Ragauskas, A. J. Stereolithography 3D Printing of Lignin-Reinforced Composites with Enhanced Mechanical Properties. *ACS Omega* **2019**, *4* (23), 20197–20204. https://doi.org/10.1021/acsomega.9b02455.

(29) Curran, M. A. Bio-Based Materials. In *Kirk-Othmer Encyclopedia of Chemical Technology*; John Wiley & Sons, Inc.,: Hoboken, 2010. https://doi.org/10.1002/0471238961.supewang.a01.
(30) European Commission. *Mandate Addressed to CEN, CENELEC and ETSI for the Elaboration of a Standardisation Programme for Bio-Based Products - M429*; 2008.
(31) Rouquerol, J.; Llewellyn, P.; Rouquerol, F. Is the Bet Equation Applicable to Microporous Adsorbents? In *Studies in Surface Science and Catalysis*; Llewellyn, P. L., Rodriquez-Reinoso, F., Rouqerol, J., Seaton, N., Eds.; Characterization of Porous Solids VII; Elsevier, 2007; Vol. 160, pp 49–56. https://doi.org/10.1016/S0167-2991(07)80008-5.
(32) Thommes, M.; Kaneko, K.; Neimark, A. V.; Olivier, J. P.; Rodriguez-Reinoso, F.; Rouquerol, J.; Sing, K. S. W. Physisorption of Gases, with Special Reference to the Evaluation of Surface Area and Pore Size Distribution (IUPAC Technical Report). *Pure and Applied Chemistry* **2015**, *87* (9–10), 1051–1069. https://doi.org/10.1515/pac-2014-1117.
(33) Jagiello, J.; Olivier, J. P. Carbon Slit Pore Model Incorporating Surface Energetical Heterogeneity and Geometrical Corrugation. *Adsorption* **2013**, *19* (2), 777–783. https://doi.org/10.1007/s10450-013-9517-4.
(34) Nicollin, A.; Zhou, X.; Pizzi, A.; Grigsby, W.; Rode, K.; Delmotte, L. MALDI-TOF and 13C NMR Analysis of a Renewable Resource Additive—Thermoplastic Acetylated Tannins. *Industrial Crops and Products* **2013**, *49*, 851–857. https://doi.org/10.1016/j.indcrop.2013.06.013.
(35) Grigsby, W. J.; Bridson, J. H.; Lomas, C.; Elliot, J.-A. Esterification of Condensed Tannins and Their Impact on the Properties of Poly(Lactic Acid). *Polymers* **2013**, *5* (2), 344–360. https://doi.org/10.3390/polym5020344.
(36) Konai, N.; Raidandi, D.; Pizzi, A.; Girods, P.; Lagel, M.-C.; Kple, M. Thermogravimetric Analysis of Anningre Tannin Resin. *Maderas, Cienc. tecnol.* **2016**, No. ahead, 0–0. https://doi.org/10.4067/S0718-221X2016005000022.
(37) Krongauz, V. V. Crosslink Density Dependence of Polymer Degradation Kinetics: Photocrosslinked Acrylates. *Thermochimica Acta* **2010**, *503–504*, 70–84. https://doi.org/10.1016/j.tca.2010.03.011.
(38) Celzard, A.; Fierro, V. "Green", Innovative, Versatile and Efficient Carbon Materials from Polyphenolic Plant Extracts. *Carbon* **2020**, *167*, 792–815. https://doi.org/10.1016/j.carbon.2020.05.053.
(39) Tondi, G.; Petutschnigg, A. Middle Infrared (ATR FT-MIR) Characterization of Industrial Tannin Extracts. *Industrial Crops and Products* **2015**, *65*, 422–428. https://doi.org/10.1016/j.indcrop.2014.11.005.
(40) Roux, D. G.; Ferreira, D.; Hundt, H. K.; Malan, E. Structure, Stereochemistry, and Reactivity of Natural Condensed Tannins as Basis for Their Extended Industrial Application. *Appl. Polym. Symp.* **1975**, *28*, 335–353.
(41) Beda, A.; Taberna, P.-L.; Simon, P.; Matei Ghimbeu, C. Hard Carbons Derived from Green Phenolic Resins for Na-Ion Batteries. *Carbon* **2018**, *139*, 248–257. https://doi.org/10.1016/j.carbon.2018.06.036.
(42) Beda, A.; Escamilla-Pérez, A. M.; Simonin, L.; Matei Ghimbeu, C. Vegetal-Extracted Polyphenols as a Natural Hard Carbon Anode Source for Na-Ion Batteries. *ACS Appl. Energy Mater.* **2022**, *5* (4), 4774–4787. https://doi.org/10.1021/acsaem.2c00215.
(43) Tonnoir, H.; Huo, D.; Canevesi, R. L. S.; Fierro, V.; Celzard, A.; Janot, R. Tannin-Based Hard Carbons as High-Performance Anode Materials for Sodium-Ion Batteries. *Materials Today Chemistry* **2022**, *23*, 100614. https://doi.org/10.1016/j.mtchem.2021.100614.
(44) Seifi, A.; Bahramian, A. R.; Sharif, A. Correlation between Structure and Oxidation Behavior of Carbon Aerogels. *Journal of Energy Storage* **2016**, *7*, 195–203. https://doi.org/10.1016/j.est.2016.07.003.
(45) Tomaši, V.; Brnardi, I.; Jenei, H.; Kosar, V.; Zrnèevi, S. Combustion of Active Carbon as a Model Carbon Material: Comparison of Non-Catalytic and Catalytic Oxidation. *Chem. Biochem. Eng. Q.* **2011**, 6.

(46) Chaparro-Garnica, C. Y.; Davó-Quiñonero, A.; Bailón-García, E.; Lozano-Castelló, D.; Bueno-López, A. Design of Monolithic Supports by 3D Printing for Its Application in the Preferential Oxidation of CO (CO-PrOx). *ACS Appl. Mater. Interfaces* **2019**, *11* (40), 36763–36773. https://doi.org/10.1021/acsami.9b12731.
(47) Chaparro-Garnica, C. Y.; Bailón-García, E.; Lozano-Castelló, D.; Bueno-López, A. Design and Fabrication of Integral Carbon Monoliths Combining 3D Printing and Sol–Gel Polymerization: Effects of the Channel Morphology on the CO-PROX Reaction. *Catal. Sci. Technol.* **2021**, *11* (19), 6490–6497. https://doi.org/10.1039/D1CY01104A.
(48) Chaparro-Garnica, C. Y.; Bailón-García, E.; Davó-Quiñonero, A.; Lozano-Castelló, D.; Bueno-López, A. Sponge-like Carbon Monoliths: Porosity Control of 3D-Printed Carbon Supports and Its Influence on the Catalytic Performance. *Chemical Engineering Journal* **2022**, *432*, 134218. https://doi.org/10.1016/j.cej.2021.134218.
(49) Llamas-Unzueta, R.; Menéndez, J. A.; Suárez, M.; Fernández, A.; Montes-Morán, M. A. From Whey Robocasting to Custom 3D Porous Carbons. *Additive Manufacturing* **2022**, *59*, 103083. https://doi.org/10.1016/j.addma.2022.103083.
(50) Du, J.; Li, W.-C.; Ren, Z.-X.; Guo, L.-P.; Lu, A.-H. Synthesis of Mechanically Robust Porous Carbon Monoliths for CO2 Adsorption and Separation. *Journal of Energy Chemistry* **2020**, *42*, 56–61. https://doi.org/10.1016/j.jechem.2019.06.006.
(51) Gupta, S.; Dey, M.; Javaid, S.; Ji, Y.; Payne, S. On the Design of Novel Biofoams Using Lignin, Wheat Straw, and Sugar Beet Pulp as Precursor Material. *ACS Omega* **2020**, *5* (28), 17078–17089. https://doi.org/10.1021/acsomega.0c00721.
(52) Seraji, M. M.; Arefazar, A. Thermal Ablation-Insulation Performance, Microstructural, and Mechanical Properties of Carbon Aerogel Based Lightweight Heat Shielding Composites. *Polymer Engineering & Science* **2021**, *61* (5), 1338–1352. https://doi.org/10.1002/pen.25648.
(53) Gibson, L. J.; Ashby, M. F. *Cellular Solids: Structure and Properties*, 2nd ed.; Cambridge University Press, 1997. https://doi.org/10.1017/CBO9781139878326.
(54) Castro-Gutiérrez, J.; Palaimiene, E.; Macutkevic, J.; Banys, J.; Kuzhir, P.; Schaefer, S.; Fierro, V.; Celzard, A. Electromagnetic Properties of Carbon Gels. *Materials* **2019**, *12* (24), 4143. https://doi.org/10.3390/ma12244143.
(55) Gabhi, R.; Basile, L.; Kirk, D. W.; Giorcelli, M.; Tagliaferro, A.; Jia, C. Q. Electrical Conductivity of Wood Biochar Monoliths and Its Dependence on Pyrolysis Temperature. *Biochar* **2020**, *2* (3), 369–378. https://doi.org/10.1007/s42773-020-00056-0.
(56) Yang, L.; Takkallapally, C.; Gabhi, R. S.; Jiang, W.; Kirk, D. W.; Jia, C. Q. Wood Biochar Monolith-Based Approach to Increasing the Volumetric Energy Density of Supercapacitor. *Ind. Eng. Chem. Res.* **2022**, *61* (23), 7891–7901. https://doi.org/10.1021/acs.iecr.2c00447.
(57) Szczurek, A.; Fierro, V.; Plyushch, A.; Macutkevic, J.; Kuzhir, P.; Celzard, A. Structure and Electromagnetic Properties of Cellular Glassy Carbon Monoliths with Controlled Cell Size. *Materials* **2018**, *11* (5), 709. https://doi.org/10.3390/ma11050709.
(58) Soukup, L.; Gregora, I.; Jastrabik, L.; Koňáková, A. Raman Spectra and Electrical Conductivity of Glassy Carbon. *Materials Science and Engineering: B* **1992**, *11* (1–4), 355–357. https://doi.org/10.1016/0921-5107(92)90240-A.

675 GRAPHICAL ABSTRACT

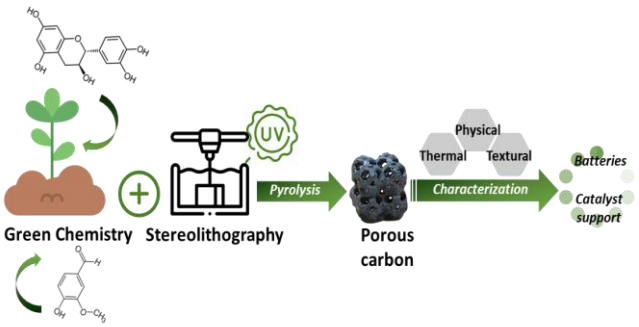

676

677

678 SYNOPSIS

679 3D-printed bio-based carbon with improved mechanical and oxidation properties were produced

680 from chemically functionalized vanillin and tannin.